

Texture tomography with high angular resolution utilizing sparsity

Mads Carlsen^a, Florencia Malamud^a, Peter Modregger^{d,e}, Anna Wildeis^f, Markus Hartmann^f, Robert Brandt^f, Andreas Menzel^a, and Marianne Liebi^{a,b,c}

^aPaul Scherrer Institut, 5232 Villigen PSI, Switzerland

^bDepartment of Physics, Chalmers University of Technology, SE-412 96 Gothenburg, Sweden

^cInstitute of Materials, Ecole Polytechnique Fédérale de Lausanne, 1015 Lausanne, Switzerland

^dPhysics department, University of Siegen, 57072 Siegen, Germany

^eCenter for X-ray and Nano Science CXNS, Deutsches Elektronen-Synchrotron DESY, 22607 Hamburg, Germany

^fMechanical Engineering Department, University of Siegen, 57072 Siegen, Germany

June 2024

Abstract

We demonstrate a novel approach to the reconstruction of scanning probe x-ray diffraction tomography data with anisotropic polycrystalline samples. The method involves reconstructing a voxel map containing an orientation distribution function in each voxel of an extended 3D sample. This method differs from existing approaches by not relying on a peak-finding and is therefore applicable to sample systems consisting of small and highly mosaic crystalline domains that are not handled well by existing methods. Samples of interest include bio-minerals and a range of small-grained microstructures common in engineering metals. By choosing a particular kind of basis functions, we can effectively utilize non-negativity in orientation-space for samples with sparse texture. This enables us to achieve stable solutions at high angular resolutions where the problem would otherwise be under determined. We demonstrate the new approach using data from a shot peened martensite sample where we are able to map the twinning micro structure in the interior of a bulk sample without resolving the individual lattice domains. We also demonstrate the approach on a piece of gastropod shell with a mosaic micro structure.

1 Introduction

X-ray diffraction techniques play an irreplaceable role in the characterization of micro structure whenever bulk properties are of interest. Apart from neutron methods, the high penetration power of x-rays are unmatched by other structural probes that are therefore limited to studying thin samples and surfaces. While traditional x-ray diffraction techniques probe the volume-averaged structure of extended samples, a range of tomographic techniques have been developed that yield spatially resolved information.

In this paper, we present a new approach for analysing the data from x-ray diffraction computed tomography (XRD-CT)[1, 2, 3] experiments resulting in a spatially resolved 3D map of the texture of a polycrystalline sample. By utilizing a non-negativity constraint in orientation space, we achieve stable reconstructions of strongly textured materials even when the linear system of equations solved is highly under determined.

The proposed method extends the principles of tensor tomography[4, 5, 6] and is formally identical to the method developed by Frewein et al.[7] called texture tomography except with a different choice of basis functions. The choice of basis functions taken in this paper allows us to enforce the prior knowledge of sparsity on the solution which is necessary to ensure unique solutions at high angular resolution. As texture tomography and the method proposed in this paper reconstruct the orientation distribution function (ODF) in each voxel whereas the established tensor tomography techniques reconstruct pole figures, we introduce the abbreviations ODF-TT and PF-TT to distinguish between them in this paper.

Our method is similar to scanning three-dimensional x-ray diffraction (s3D-XRD)[8, 9, 10] which uses the same measurement approach but aims to reconstruct the orientation field rather than the ODF. More generally, the proposed method falls within a large family of x-ray techniques which are collectively referred to as three-dimensional x-ray diffraction (3D-XRD)[11] which contains s3D-XRD[8] as well as a number of full-field techniques[12, 13, 14, 15, 16, 17]. However, the tensor/textture tomography approaches significantly differ from the established techniques in that they do not rely on spatially resolving the smallest coherent lattice domains of the sample (be it grains, sub-grains, or twin domains) but are able to reconstruct the spatially averaged texture over many crystalline domains. Therefore the techniques are suitable for a range of small-grained and highly deformed materials such as boneapatite[18, 19] and cold-worked

metals[20].

ODF-TT overcomes some of the weaknesses of other x-ray scattering-tomography techniques and opens up possibilities for investigating samples, not covered by existing techniques. By reconstructing the full ODF using grid based basis functions to expand the ODFs, non-negativity in orientation-space can be enforced, overcoming certain ambiguities of the inversion problem. Furthermore, by enforcing the lattice symmetries we overcome the ‘missing wedge’ problem of PF-TT[6, 21] allowing experiments to be carried out in a simpler geometry without a second tilt rotations stage which is commonly used in PF-TT. We first present the mathematical approach to the reconstruction and then apply the method to a 2D XRD-CT dataset from a piece of shot-peened martensite and to a full 3D tensor-tomography dataset of a piece of gastropod shell.

2 Method

For a thorough introduction to the methodology of TT, we refer to papers on the subject such as [22] and [7] that both utilize a model and geometry similar to the one applied here. The methods arise naturally by combining established approaches from texture inversion and computed tomography. We first present some of the key results of texture inversion and then describe how the tomographic problem is constructed and solved.

2.1 Texture inversion

While tensor tomography was originally applied for small angle x-ray scattering[5, 6](SAS-TT), its extension to wide-angle Bragg scattering is straightforward[18, 20]. In SAS-TT, the reconstructed quantity is called the reciprocal space map. For crystalline systems displaying scattering only in discrete shells corresponding to the length of reciprocal lattice vectors of the lattice, the reciprocal space map on such a sphere is called a pole figure. These pole figures have to follow symmetries corresponding to the rotational symmetries of the crystal lattice. However, the symmetries are not fully realized in the individual pole figures but result in correlations between different pole figures. This motivates the reconstruction of a different quantity, the ODF which describes the anisotropy of all Bragg peaks simultaneously and allows the rotational symmetries to be included.

The reconstruction of the ODF from x-ray diffraction measurements is called texture inversion. Like computed tomography, texture inversion is an inverse problem that revolves around reconstructing a 3-dimensional function from a series of measurements of 2-dimensional projections. In computed tomography, this projection is defined by the well-known Radon- or x-ray transform in Cartesian coordinates. In texture inversion, the projection operation is given by a similar integral equation that relates a pole figure defined on the two dimensional space of directions to an ODF

defined on the three dimensional space of proper rotations.

Texture inversion problems are most commonly analyzed using the harmonic method, in which the ODF is expanded in a series of generalized spherical harmonics[23, 24]. One of the most important properties of the harmonic expansion in this regard is that the projection operator applied to the generalized spherical harmonics of a given order ℓ are projected onto spherical harmonics of the same order in the spherical harmonics expansion of pole figures. This property allows splitting the inversion into independent problems for each order ℓ and provides explicit quadrature equations to determine the coefficients of the ODF when complete measurements of the pole figures are available[24].

However, the harmonic method of texture inversion suffers from reconstruction artifacts termed the ghost problem[25]. This issue arises because the ODF generally consists of both even- ℓ and odd- ℓ terms in the harmonic expansion, but odd terms of the pole figures cannot be measured by x-ray diffraction due to Friedel’s law which causes inversion symmetry of the measured pole figures.

To overcome this shortcoming, a different family of methods were developed starting from the late seventies. These methods expand the ODF in a series of localized functions centered on a grid of orientations that maps the asymmetric zone of the crystal lattice. These functions are typically either: (1) the indicator-functions of some partition of the asymmetric zone, resulting in a piecewise-constant approximation of the ODF[26, 27], (2) finite elements, which gives a piecewise linear approximation[28], or (3) spherically symmetric standard-functions[29] such as a spherical Gaussian function used in this work. While this change of basis does not eliminate the ghost problem, it makes it easier to enforce certain kinds of prior knowledge and to compute regularized solutions[30] that can alleviate the problem. For sparse textures, where the ODF is close to or equal zero in extended regions of orientation space, the non-negativity constraint has been observed to resolve the inherent ambiguity of the texture inversion problem[31, 32].

2.2 The tomographic problem

To write up the tomographic problem, we expand the pole figure of the voxel at position x, y, z as a series expansion of ODF basis functions:

$$O_{xyz}(g) = \sum_{\mu} c_{xyz\mu} O_{\mu}(g) \quad (1)$$

where $c_{xyz\mu}$ are the unknown expansion coefficients, g is a proper rotation, and $O_{\mu}(g)$ are the basis functions. The ODF defined by this expression is not properly normalized and the reconstructed quantity is actually the density of the crystalline phase times the ODF.

For each ODF basis function, we can pre-compute the corresponding pole-figure values at the points given

by the geometry of the experiment. These values are stored in a set of matrices with elements:

$$B_{ch}^{\mu}(R_i) = \mathcal{P}_h\{O_{\mu}\}(R_i^{\top} \mathbf{q}_{hc}), \quad (2)$$

where $\mathcal{P}_h\{\cdot\}$ is the pole figure projection operator in ODF space, R_i denotes the setting of the rotation stage, and \mathbf{q}_{hc} is the scattering vector measured by detector segment at the azimuthal channels labeled by c , and the Bragg peak labeled by h . These matrix coefficients can be computed with standard approaches from texture inversion and open-source software packages[33].

The full tomographic problem can now be written as

$$I_{chjk}(R_i) = \sum_{xyz} P_{jk}^{xyz}(R_i) \sum_{\mu} B_{ch}^{\mu}(R_i) c_{xyz\mu}, \quad (3)$$

where $I_{chjk}(R_i)$ is the 5-dimensional dataset containing the integrated intensities and $P_{jk}^{xyz}(R_i)$ are the matrix elements of the discrete x-ray transform that transforms the voxel-grid (x, y, z) to the coordinates of the raster-scan grid (j, k) . In a 2D geometry, the indices y and k can be omitted and P is the Radon transform. To write the problem in this form, we have assumed that the scaling-factors that describe the relative intensity of different Bragg peaks are known beforehand and have been normalized out of the measured intensities which is needed to write the forward model in this linear form[33].

We rewrite the model with linear algebra syntax as

$$\mathbf{I} = \mathbf{Ac} \quad (4)$$

by flattening the data set into a single vector \mathbf{I} , the expansion coefficients into a vector \mathbf{c} and the products of $P_{jk}^{xyz}(R_i)$ and $B_{ch}^{\mu}(R_i)$ into a single matrix \mathbf{A} . This forms a large system of linear equations that will typically be under determined when the ODF-expansion is performed to high angular resolution. Here, we will focus on textured materials, where the ODF is close to zero in large regions of orientation space. This adds the prior knowledge needed to overcome the inherent ambiguities of the inversion problem. To find the solution we minimize the square residual with L1 regularization. In the experiments shown here, the regularization is not critical to ensure convergence to a stable solution, but can help suppress reconstruction artifacts. (See supplementary information.)

$$\begin{aligned} \mathbf{c}_{\text{Opt}} = \underset{\mathbf{c}}{\text{argmin}} & \|\mathbf{I} - \mathbf{Ac}\|_2^2 + \lambda \|\mathbf{c}\|_1 \\ \text{s.t. } & c_{xyz\mu} \geq 0 \quad \forall x, y, z, \mu, \end{aligned} \quad (5)$$

where λ is a regularization parameter and $\|\cdot\|_n$ denotes the Euclidean and 1-norm for n equals 2 and 1 respectively. To solve this optimization problem, we use projected gradient descent with Nesterov momentum.

Similar to texture inversion, reconstruction of tensor tomography also suffers from ambiguities that are

due to the experimental difficulty of properly sampling the full range projection directions. While standard computed tomography problems can be inverted using projections measured around a single rotation axis, PF-TT requires sampling of the full half unit sphere of possible projection directions to be solvable. This necessitates the inclusion of a second tilt stage in the experimental set up and causes longer measurement times. Even with such a sample stage, a range of projection angles are usually obfuscated by the sample holder which leads to the so-called missing wedge problem in PF-TT due to which certain Fourier components of certain scattering directions cannot be probed[6, 21]. While it can be shown that full angular sampling is necessary when different scattering directions are reconstructed independently[6], it is less clear if this is necessary when using a model that enforces correlations between different scattering directions. This has lead several authors to assert that PF-TT is possible with such methods[34, 35] despite systematic studies generally showing this to have a negative impact on the quality of the reconstructions[36, 20].

As we will show here, ODF-TT is able to overcome the missing wedge problem of PF-TT and achieve solutions without a tilt rotation by utilizing the extra information given by the lattice symmetry and the sparse texture.

3 Experiment

To test the feasibility of ODF-based TT, we show results using two separate experimental datasets. One is a piece of martensitic steel which is a sample system of high scientific interest and with a well known twinned microstructure that has so far not been possible to map with 3D-XRD approaches. The other is a biomimetic sample where a full 3D tensor tomography data set is available to allow us to compare the performance of ODF-TT with PF-TT. Fig. 1a,b) shows examples of raw detector frames from each of these two data sets. Both data sets display strongly anisotropic Debye-Scherrer rings but lack easily identifiable separate diffraction spots.

3.1 Shot-peened martensite

The first sample is a piece of martensitic steel with a cross section of about 0.8 mm by 1 mm. The sample was shot-peened from three sides in order to introduce high residual stresses and varying crystallite sizes from the edges to the center.

The experiment was carried out at the P21.2 beamline [37] of PETRA III (Hamburg, Germany). A photon energy of 68 keV was selected by a double Laue monochromator. Compound refractive lenses shaped a pencil beam of 8 μm width by 3 μm height with a photon flux of about 10^{10} photons per second. A VAREX XRD4343CT detector with a pixel size of 150 μm was positioned about 0.8 m downstream of the sample and provided diffraction angles of up to $2\theta_{\text{max}} = 14^\circ$.

Shot-peened Martensite

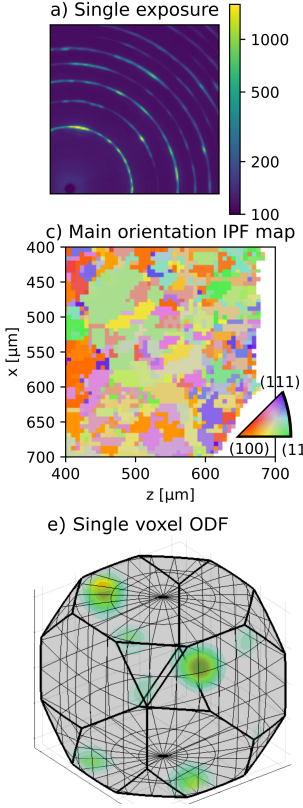
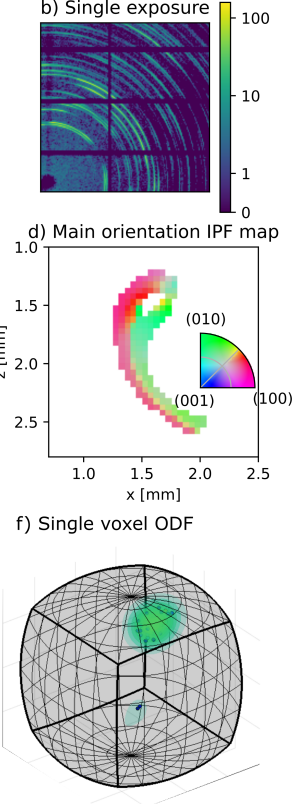


Figure 1: Examples of data frames and reconstructions. a,b) show examples of raw detector frames used to create the ODF-TT reconstructions. c,d) show 2D slices of the reconstructed primary orientations plotted as inverse pole figure maps. e,f) show the ODFs of example voxels of the reconstructions plotted as densities in three-dimensional axis angle space within the asymmetric zone of the e) cubic and f) orthogonal lattices respectively. a,c,e) are from the shot-peened martensite sample and b,d,f) are from the gastropod shell sample.

Gastropod shell



The single rotation axis was oriented in vertical direction. The sample was scanned with stepwise translations orthogonal to the rotation axis and continuous rotation. In total, 200 projections were collected over 360° and the sample was translated 200 times in $8\text{ }\mu\text{m}$ steps, which resulted in a field of view of 1.6 mm . The exposure time was 0.4 s and a total number of 40 000 frames were acquired, which took approximately 5 h.

The integrated intensity was determined for each of the seven diffraction rings that were fully captured by the detector and azimuthally regrouped into 72 equally spaced azimuthal bins. The resulting sinograms were corrected by the absorption signal provided by a beamstop diode.

The reconstruction was performed without regularization by running the algorithm for 1000 iterations which took 8 hours to complete. The 2D slice was reconstructed on a 150×150 pixel grid with an ODF expansion using 10 000 orientations in the asymmetric zone. For each orientation a spherically symmetric Gaussian with $\sigma = 0.05\text{ rad}$ was used. This gives 15 million data points and 240 million degrees of freedom of which 0.6 million were non-zero in the converged solution. The final reconstruction has an R^2 value of 0.8.

3.2 Gastropod shell

The second sample consists of a piece of the shell of a *helix pomatia* (Roman snail) which was found, already dead and without traces of the soft body remaining, in the forests near Beznau, Aargau, Switzerland. A small piece measuring $3\text{ mm} \times 3\text{ mm} \times 2\text{ mm}$ of the columella was taken about 5 mm below the apex. The snail shell consists mainly of aragonite and no other crystalline components could be identified in the diffraction patterns.

The sample was measured the cSAXS beamline at the Swiss Light Source. The experiments were performed with a photon energy of 18 keV and a sample-to-detector distance of 0.2 m using a Pilatus 2M detector. The beam was focused to a spot of approximately $50\text{ }\mu\text{m} \times 50\text{ }\mu\text{m}$ and the sample was raster-scanned in 2D through the focused beam with continuous translations in one direction and a step-size of $50\text{ }\mu\text{m}$ and step-scanning with two orthogonal rotation stages. The intensity of the direct beam was measured on the image-detector behind a semi-transparent beamstop constructed of several small discs of single-crystal silicon glued together.

For this sample, a full TT-dataset was measured, containing measurement made at tilt angles extending up to 45° . This allows the texture to be reconstructed with the more established PF-TT approach and the two approaches to be compared as well as a comparison between using the full data set and using a zero-tilt geometry only.

The diffraction patterns contain 16 rings that are fully covered by the detector but due to partial overlaps of some peaks, only eight rings were used for the reconstructions. These rings were azimuthally regrouped

into 96 equally spaced bins.

For the reconstructions, we use a grid of 8 000 orientations and Gaussian functions with width $\sigma = 0.1$ rad for the basis set. The gastropod shell consists of aragonite of the orthohombic crystal class which means the rotation group contains only 4 symmetries compared to the 24 in the cubic crystal class of ferrite. Therefore, even though the number of grid orientations are similar, the angular resolution of the gastropod shell reconstruction is about a factor of two worse than the martensite reconstruction. The full three dimensional problem has 600 million data points hereof 150 million in the zero tilt part and the model uses 1.8 billion degrees of freedom.

4 Results

Figure 2 shows a number of quantities computed from the reconstruction of the martensite data set. In Fig. 2a,b) we see that the shape of the sample is well reconstructed and that the reconstructed density is fairly homogeneous as expected for the sample which consists almost entirely of ferrite. In Fig. 2c) we display the texture index of the individual voxels. The texture index $J_{xyz} = \langle c_{xyz\mu}^2 \rangle_\mu / \langle c_{xyz\mu} \rangle_\mu^2$ is a measure of the sharpness of the texture which is equal to one for a random (uniform) texture and increases towards infinity for a single crystal. We observe that the shot-peened surfaces (that is, all surfaces except the straight edge at the top of the figure) display a markedly lower texture index than the rest of the sample. This observation is highlighted in Fig. 2d). Using the ODF mode with the highest coefficient in each voxel, we determine a main orientation in each voxel. But as is shown in 2e), only about half of the total intensity can be attributed to this main orientation. This finding shows that coherent lattice domains do not extend over the length scale resolved by this experiment. The domains observed in the reconstruction are rather parent grains or martensite packets. Fig. 2e) shows the main orientation plotted as an inverse pole figure map. Some large domains of sizes up to 50 μm are present, but regions with domains down to the resolution of the experiment are also observed.

In Fig. 3 we zoom in and provide a view of the texture within single voxels. After subtracting the components within a 20° radius of the main orientation, we can compute a second and third main orientation using the same approach. As can be seen from Fig. 3c,d), the local texture is often dominated by three distinct orientations that appear at large misorientation angles to each other. For the two selected pixels, we see that the pixel near the peened surface has more diffuse intensity away from the major peaks. This is interpreted to be due to deformation twinning, stemming from the peening process.

To quantify the twinning in the sample, we calculate the misorientation between the primary and secondary orientations for each voxel. Fig. 3 e) shows the distribution of the direction of the misorientation axis in

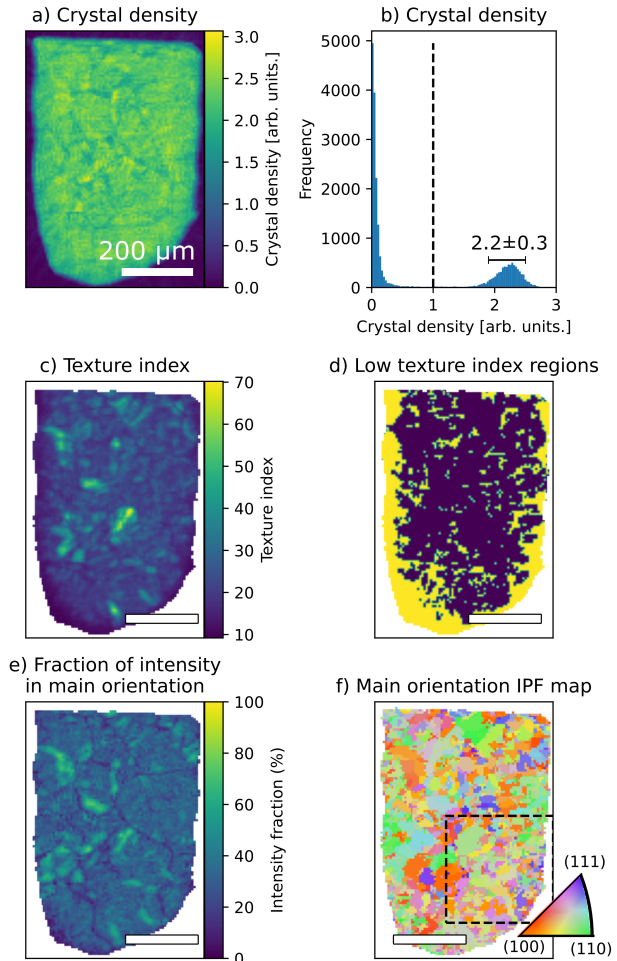


Figure 2: Reconstructed tomogram of the steel-sample. a) crystal density, b) histogram of the reconstructed density values. The dashed line marks the threshold used to generate the mask distinguishing sample and air. c) approximate texture index computed from the standard deviation of the reconstructed coefficients of each pixel d) a binarized map showing regions with texture-index lower than 20 in yellow e) fraction of the ODF-density that falls within a sphere of radius 20° of the main-orientation. f) Main orientation determined as the grid orientation with the largest coefficient in each voxel.

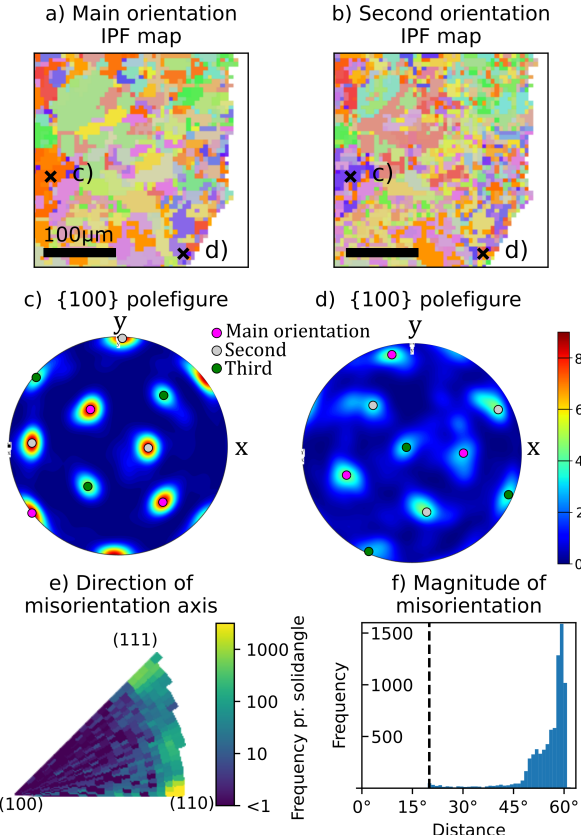


Figure 3: Zoomed-in view of the region of the martensite sample marked in 2f). Inverse pole figure maps of the a) primary and b) secondary orientations. c,d) show the {100} pole figures of 2 selected pixels, marked in a) and b). Overlaid on these pole figures are the poles corresponding to the three main orientations. Histograms of the e) direction of the misorientation axis between the primary and secondary orientations in lattice coordinates and f) the magnitude of the misorientation.

the lattice coordinates. We see that the misorientation is mainly around $\langle 110 \rangle$ directions and directions close to, but not quite aligned with $\langle 111 \rangle$. Fig.3 f) shows the magnitude of the misorientation. The way we calculated the secondary orientations precludes the observation of misorientations with magnitude smaller than 20° , but beyond this, almost no misorientations between 20° and 45° are detected. The found directions and magnitudes of the misorientations are consistent with the three Bain groups expected in martensitic transformation twinning[38, 39].

For the gastropod sample, ODF-TT achieved good reconstructions without regularization, but using L1-norm regularization can reduce streaking artifacts. The local micro structure is dominated by a single orientation with a mosaic spread of around 20° FWHM and the crystallographic c -axis aligned with the surface normal of the columellar wall, typical for prismatic aragonite shells in mollusks[40]. Fig. 4 a) shows a 3D rendering of the reconstruction using the full dataset displaying the main direction of the c -axis. The main orientation was computed by first selecting the basis set mode with the largest coefficient for each voxel and then computing the center of mass in a tangent space centered on this maximum weight orientation. Fig. 4 b,c) shows a single slice of the reconstruction using respectively the full data set and the zero-tilt data set.

The gastropod shell data set can also be reconstructed using established techniques from PF-TT. To give a fair comparison, we use a set of basis functions similar to the ones used in the ODF-TT reconstructions consisting of symmetric Gaussian functions placed on a grid of directions covering the half-sphere[21] which can also benefit from the non-negativity constraint and sparse texture. To facilitate comparison between the two reconstruction methods, we chose to reconstruct the 200 Bragg peak which has multiplicity 2 and from which we can therefore easily compute a main direction. The reconstructions were performed using the software package `mumott`[41].

Fig. 5 shows a comparison between the ODF-TT reconstruction and the PF-TT reconstruction. OFT-TT reconstructs a smoothly varying direction both with the full and zero-tilt data sets except where the columnar wall touches itself after folding around the umbilical. These two sheets have distinct orientations, sharing only the c -axis, as can be more clearly seen from the inverse pole figure map Fig.1 d) which is not unexpected since they were grown at two different points in the lifetime of the snail. The direction found from the PF-TT reconstructions on the other hand has sudden variations along the columnar wall and appears more erratic. With the full dataset, the PF-TT direction is close to the ODF-TT directions at many points in the sample, especially near the center where the sample is thicker, but differs significantly at the narrower features. This is consistent with the type of ‘missing wedge’ artifacts common in PF-TT where plane-like features are difficult to reconstruct when the projections orthogonal to the normal of the plane have not been measured. With only the zero tilt data, there

are no longer any clear correlation between the direction of the PF-TT reconstruction and of the ODF-TT reconstructions.

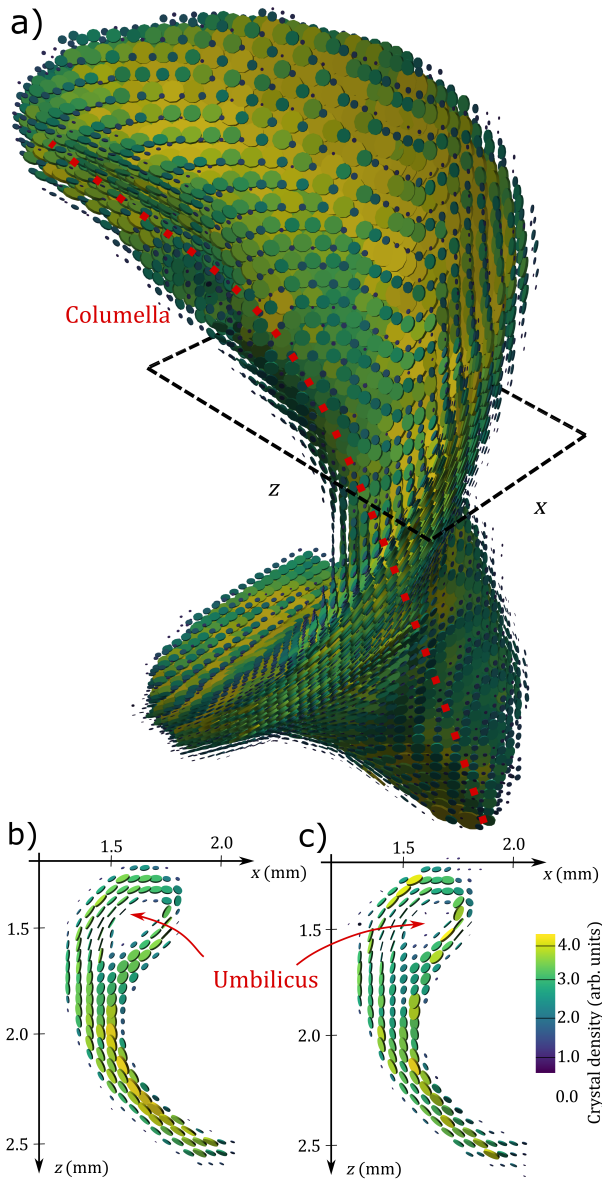


Figure 4: 3D renders of the reconstructed snail-shell sample using ODF-based TT. The reconstruction is displayed using flat cylinder shaped glyphs. The color and size of each glyph is determined by the crystal density and perspective shading and lighting is sense of orientation. The direction of the faces are aligned with the c -axis direction of the main orientation. a) shows the full volume of the reconstructions. b,c) show a single slice thorough the middle of the reconstruction marked with a dashed outline in b) using the full data set and c) zero tilt part respectively.

5 Discussion

Different versions of volumetric grain-mapping synchrotron x-ray techniques have existed for more than twenty years[12]. However, they are mostly limited to either materials with low intragranular strain or samples with a small number of grains. Recent advances have targeted larger strains by utilizing a focused beam[8], conical slits[42], or by improved computational approaches[43]. Still these approaches have so far only been demonstrated on fairly simple grain structures. Martensite and other highly strained phases, which Hayashi et al. refers to as ‘invisible phases’[44], have thus far not been possible to reconstruct with 3DXRD techniques.

Vigano et al.[16] showed that the 3DXRD problem could be linearized by writing the problem as a search for a distribution in six-dimensional orientation-position space rather than an orientation field. However, this approach has not been applied to the scanning beam geometry and still depends on an initial peak-finding step. Dark-field x-ray microscopy[45] and differential aperture x-ray microscopy[46, 47] have both been used to image highly deformed microstructures in the bulk of extended samples[48, 49] but work with smaller volumes and at higher angular and spatial resolution.

The aim of ODF-TT is less ambitious than many of the existing 3D-XRD techniques, as it does not aim to reconstruct the individual grains or the strain field and has worse angular resolution. However, compliments these techniques due to its simplicity and ability to study less well ordered materials such as twinned and highly strained microstructures that are of clear technological importance.

The output of an ODF-TT reconstruction is a large number of ODFs, and both analysis and visualization of the reconstruction is challenging. For a sample such as the gastropod snail, where a main orientation can be defined, the information contained in ODFs can be reduced to a small number of derived quantities, such as the orientation field, density and mosaic spread. For more complex and not fully resolved microstructures such as the martensite, more complicated analysis is required to make sense of the reconstructions. This involves processes such as martensite packet and parent grain determination[50]. While the field of texture analysis provides methods for these tasks, they are typically designed for different settings. In electron back scatter diffraction(EBSD) images, the orientation field is well resolved and the task involves grouping neighboring pixels based on their relative misorientations. Traditional x-ray texture mapping on the other hand relies on a high-angular resolution texture map of the entire sample to be known. In summary, existing algorithms need to be adapted for in-depth analysis ODF-

TT reconstructions.

6 Conclusion

We have demonstrated a novel approach for tomographic 3D mapping of crystallographic texture in extended samples using a method similar to pole-figure based tensor tomography. By utilizing grid based basis functions and leveraging sparsity, we can overcome the inherent ambiguities of the inversion problem. Our proof-of-principle experiments show that a reconstruction can be achieved even for highly under-constrained problems by applying a non-negativity constraint in samples with locally sparse textures.

Unlike for PF-TT, our method achieves good reconstructions with measurements using only a single rotation axis. This means that both experiments and reconstructions can be carried out in a slice-by-slice manner which enables fast single-slice experiments with measurement times on the order of minutes rather than hours. This simplifies the experimental procedure by not requiring a second rotations stage, facilitating in-situ experiments using various existing sample environments at a range of synchrotron end stations.

Our findings suggest that ODF-TT with grid-type basis functions will be able to extend the range of samples that can be characterized with existing 3D-XRD and PF-TT techniques. This includes twinned and deformed metal microstructures and broadly mosaic biominerals.

Acknowledgments

We acknowledge the Paul Scherrer Institute, Villigen, Switzerland for provision of synchrotron beamtime at the cSAXS beamline of the SLS and we would like to thank C. Appel and M. Olson for assistance during the beamtime. We acknowledge DESY (Hamburg, Germany), a member of the Helmholtz Association HGF, for the provision of experimental facilities. Parts of this research were carried out at the beamline P21.2 of PETRA III. Funding information: MC has received funding from the European Union's Horizon 2020 research and innovation program under the Marie Skłodowska-Curie grant agreement No 884104. ML has received funding from the European research council (ERC-2020-StG 949301 MUMOTT).

7 Author contributions

M.C.: Conceptualization, Writing – original draft, Software, Formal analysis, experiment, Investigation, Visualization, Methodology F.M.: Formal analysis, Visualization, Writing – review & editing P.M.: Investigation, Resources, Formal analysis, Writing – review & editing A.W.: Resources M.H.: Resources R.B.: Resources, Supervision A.M.: Supervision, Funding acquisition, Writing – review & editing M.L.: Supervision

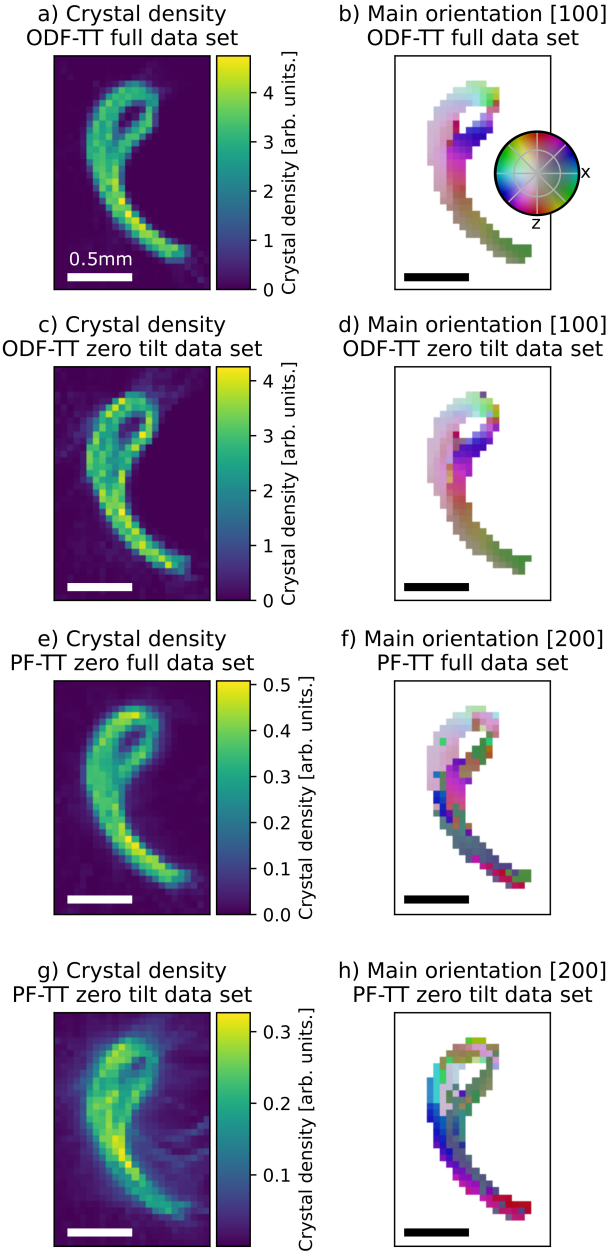


Figure 5: Comparison of reconstructions using ODF-TT and PF-TT of the gastropod shell sample. a,c,e,g) show a single slice, orthogonal to the shell axis, of the reconstructed crystal density while b,d,f,h) shows the main orientation of the (100) crystallographic direction. a,b) are from a ODF-TT reconstruction using only the full dataset with tilts up to 45° and c,d) from ODF-TT using only the zero-tilt part. e,f) are from a PF-TT reconstruction using the full data set g,h) are from a PF-TT reconstruction made using only the zero-tilt part of the data set.

sion, Funding acquisition, Methodology, Writing – review & editing

References

[1] G. Harding, J. Kosanetzky, and U. Neitzel. X-ray diffraction computed tomography. *Medical Physics*, 14(4):515–525, 1987.

[2] SR. Stock, F. De Carlo, and JD. Almer. High energy x-ray scattering tomography applied to bone. *Journal of Structural Biology*, 161(2):144–150, 2008.

[3] J. Bleuet, E. Welcomme, E. Dooryhée, J. Susini, JL. Hodeau, and P. Walter. Probing the structure of heterogeneous diluted materials by diffraction tomography. *Nature Materials*, 7:468–472, 2008.

[4] A. Malecki, G. Potdevin, T. Biernath, E. Eggli, K. Willer, T. Lasser, J. Maisenbacher, J. Gibmeier, A. Wanner, and F. Pfeiffer. X-ray tensor tomography(a). *Europhysics Letters*, 105:38002, 2014.

[5] M. Liebi, M. Georgiadis, A. Menzel, P. Schneider, J. Kohlbrecher, O. Bunk, and M. Guizar-Sicairos. Nanostructure surveys of macroscopic specimens by small-angle scattering tensor tomography. *Nature*, 527:349–352, 2015.

[6] F. Schaff, M. Bech, P. Zalansky, C. Jud, M. Liebi, M. Guizar-Sicairos, and F. Pfeiffer. Six-dimensional real and reciprocal space small-angle x-ray scattering tomography. *Nature*, 527:353–356, 2015.

[7] M. P. K. Frewein, J. K. Mason, B. Maier, H. Cölfen, M. Burghammer, A. A. Medjahed, M. Allain, and T. A. Grünwald. Texture tomography, a versatile framework to study crystalline texture in 3d, 2024.

[8] Y. Hayashi, Y. Hirose, and Y. Seno. Polycrystal orientation mapping using scanning three-dimensional x-ray diffraction microscopy. *Journal of Applied Crystallography*, 48:1094–1101, 2015.

[9] N. A. Henningsson, S. A. Hall, J. P. Wright, and J. Hektor. Reconstructing intragranular strain fields in polycrystalline materials from scanning 3dxrd data. *Journal of Applied Crystallography*, 53(2):314–325, Apr 2020.

[10] W. Li, H. Sharma, P. Kenesei, S. Ravi, H. Sehitoglu, and A. Buscek. Resolving intragranular stress fields in plastically deformed titanium using point-focused high-energy diffraction microscopy. *Journal of Materials Research*, 2023.

[11] H. Poulsen. *Three-Dimensional X-ray Diffraction Microscopy*. Springer Berlin, Heidelberg, 2004.

[12] H. F. Poulsen, S. F. Nielsen, E. M. Lauridsen, S. Schmidt, R. M. Suter, U. Lienert, L. Margulies, T. Lorentzen, and D. Juul Jensen. Three-dimensional maps of grain boundaries and the stress state of individual grains in polycrystals and powders. *Journal of Applied Crystallography*, 34(6):751–756, Dec 2001.

[13] R. M. Suter, D. Hennessy, C. Xiao, and U. Lienert. Forward modeling method for microstructure reconstruction using x-ray diffraction microscopy: Single-crystal verification. *Review of Scientific Instruments*, 77(12):123905, 12 2006.

[14] S. Schmidt, U.L. Olsen, H.F. Poulsen, H.O. Sørensen, E.M. Lauridsen, L. Margulies, C. Maurice, and D. Juul Jensen. Direct observation of 3-d grain growth in al-0.1 *Scripta Materialia*, 59(5):491–494, 2008.

[15] Wolfgang Ludwig, Søeren Schmidt, Erik Mejdal Lauridsen, and Henning Friis Poulsen. X-ray diffraction contrast tomography: a novel technique for three-dimensional grain mapping of polycrystals. I. Direct beam case. *Journal of Applied Crystallography*, 41(2):302–309, Apr 2008.

[16] N. Vigano, A. Tanguy, S. Hallais, A. Dimanov, M. Bornert, K. J. Batenburg, and W. Ludwig. Three-dimensional full-field x-ray orientation microscopy. *Scientific Reports*, 2016.

[17] J. Oddershede, J. Sun, N. Gueninchault, F. Bachmann, H. Bale, C. Holzner, and E. Lauridsen. Non-destructive characterization of polycrystalline materials in 3d by laboratory diffraction contrast tomography. *Integrating Materials and Manufacturing Innovation*, 2019.

[18] TA. Grünwald, M. Liebi, NK. Wittig, A. Johannes, T. Silkjaer, L. Rejnmark, Z. Gao, M. Rosenthal, M. Guizar-Sicairos, H. Birkedal, and M. Burghammer. Mapping the 3d orientation of nanocrystals and nanostructures in human bone: Indications of novel structural features. *Science Advances*, 6:eaba4171, 2020.

[19] TA. Grünwald, A. Johannes, NK. Wittig, J. Palle, A. Rack, M. Burghammer, and H. Birkedal. Bone mineral properties and 3d orientation of human lamellar bone around cement lines and the haversian system. *IUCrJ*, 10:189–198, 2023.

[20] Mads Carlsen, Christian Appel, William Hearn, Martina Olsson, Andreas Menzel, and Marianne Liebi. X-ray tensor tomography for small-grained polycrystals with strong texture. *Journal of Applied Crystallography*, 57(4), Aug 2024.

[21] Leonard C. Nielsen, Torne Tänzer, Irene Rodriguez-Fernandez, Paul Erhart, and Marianne Liebi. Investigating the missing wedge problem in small-angle x-ray scattering tensor tomography across real and reciprocal space. 2024.

[22] L.C. Nielsen, P. Erhart, M. Guizar-Sicairos, and M. Liebi. Small-angle scattering tensor tomography algorithm for robust reconstruction of complex textures. *Acta Crystallographica Section A*, 79(6):515–526, 2023.

[23] Ryong-Joon Roe. Description of Crystallite Orientation in Polycrystalline Materials. III. General Solution to Pole Figure Inversion. *Journal of Applied Physics*, 36(6):2024–2031, 06 1965.

[24] H.-J. (Hans Joachim) Bunge. *Mathematische Methoden der Texturanalyse : Mit 86 Abbildungen und 31 Tabellen, sowie 7 Abbildungen und 9 Tabellen im Anhang*. Akademie-Verlag, 1969.

[25] S. Matthies. On the reproducibility of the orientation distribution function of texture samples from pole figures (ghost phenomena). *physica status solidi (b)*, 92(2):K135–K138, 1979.

[26] D. Ruer and R. Baro. Méthode vectorielle d'analyse de la texture des matériaux polycristallins de réseau cubique. *Journal of Applied Crystallography*, 10(6):458–464, 1977.

[27] H. Schaeben. Analogy and duality of texture analysis by harmonics or indicators. *Journal of Scientific Computing*, 1994.

[28] Donald E. Boyce Nathan R. Barton and Paul R. Dawson. Pole figure inversion using finite elements over rodriques space. *Textures and Microstructures*, 35(2):113–144, 2002.

[29] H. Schaeben. A unified view of methods to resolve the inverse problem of texture goniometry. *Textures and Microstructures*, 1996.

[30] H. Schaeben. Entropy optimization in texture goniometry. i. methodology. *physica status solidi (b)*, 148(1):63–72, 1988.

[31] S. Matthies. *Aktuelle Probleme der quantitativen Texturanalyse*. Akademie der Wissenschaften der DDR, Dresden, Dresden, 1972.

[32] M. Dahms and H. J. Bunge. A positivity method for the determination of complete orientation distribution functions. *Textures and Microstructures*, 1988.

[33] R. Hielscher and H. Schaeben. A novel pole figure inversion method: specification of the MTEX algorithm. *Journal of Applied Crystallography*, 41(6):1024–1037, Dec 2008.

[34] F. K. Mürer, A. S. Madathiparambil, K. R. Tekseth, M. Di Michiel, P. Cerasi, B. Chattopadhyay, and D. W. Breiby. Orientational mapping of minerals in pierre shale using x-ray diffraction tensor tomography. *IUCrJ*, 8(5):747–756, 2021.

[35] Xiaoyi Zhao, Zheng Dong, Chenglong Zhang, Himadri Gupta, Zhonghua Wu, Wenqiang Hua, Junrong Zhang, Pengyu Huang, Yuhui Dong, and Yi Zhang. A step towards 6D WAXD tensor tomography. *IUCrJ*, 11(4), Jul 2024.

[36] M. Liebi, M. Georgiadis, J. Kohlbrecher, M. Holler, J. Raabe, I. Usov, A. Menzel, P. Schneider, O. Bunk, and M. Guizar-Sicairos. Small-angle x-ray scattering tensor tomography: model of the three-dimensional reciprocal-space map, reconstruction algorithm and angular sampling requirements. *Acta Crystallographica Section A*, 74:12–24, 2018.

[37] Z. Hegedüs, T. Müller, J. Hektor, E. Larsson, T. Bäcker, S. Haas, ALC Conceição, S. Gutschmidt, and U. Lienert. Imaging modalities at the swedish materials science beamline at petra iii. *IOP Conference Series: Materials Science and Engineering*, 580(1):012032, aug 2019.

[38] G. Kurdjumow and G. Sachs. Über den Mechanismus der Stahlhärtung. *Zeitschrift für Physik*, 64(5-6):325–343, May 1930.

[39] Z. Guo, C.S. Lee, and J.W. Morris. On coherent transformations in steel. *Acta Materialia*, 52(19):5511–5518, 2004.

[40] Bøggild O. B. The shell structure of the mollusks. *Det Kongelige Danske Videnskabernes Selskabs Skrifter. Naturvidenskabelig og Mathematiske Afdeling, Raekke 9*, 2:231–326, 1930.

[41] L.C. Nielsen, M. Carlsen, M. Liebi, and P. Erhart. mumott - a python library for the analysis of photon probe tensor tomography data., 2023.

[42] Yujiro Hayashi, Daigo Setoyama, Kunio Fukuda, Katsuhiro Okuda, Naoki Katayama, and Hidehiko Kimura. Scanning three-dimensional x-ray diffraction microscopy with a spiral slit. *Quantum Beam Science*, 7(2), 2023.

[43] Axel Henningsson, Mustafacan Kutsal, Jonathan P. Wright, Wolfgang Ludwig, Henning Osholm Sørensen, Stephen A. Hall, Grethe Winther, and Henning F. Poulsen. Microstructure and stress mapping in 3d at industrially relevant degrees of plastic deformation, 2024.

[44] Yujiro Hayashi and Hidehiko Kimura. Scanning three-dimensional x-ray diffraction microscopy for carbon steels. *Quantum Beam Science*, 7(3), 2023.

[45] H. Simons, A. King, W. Ludwig, C. Detlefs, W. Panteleon, S. Schmidt, F. Stöhr, I. Snigreva, A. Snigrev, and H. F. Poulsen. Dark-field x-ray microscopy for multiscale structural characterization. *Nature Communications*, 2015.

[46] W. Yang, B.C. Larson, J.Z. Tischler, G.E. Ice, J.D. Budai, and W. Liu. Differential-aperture x-ray structural microscopy: a submicron-resolution

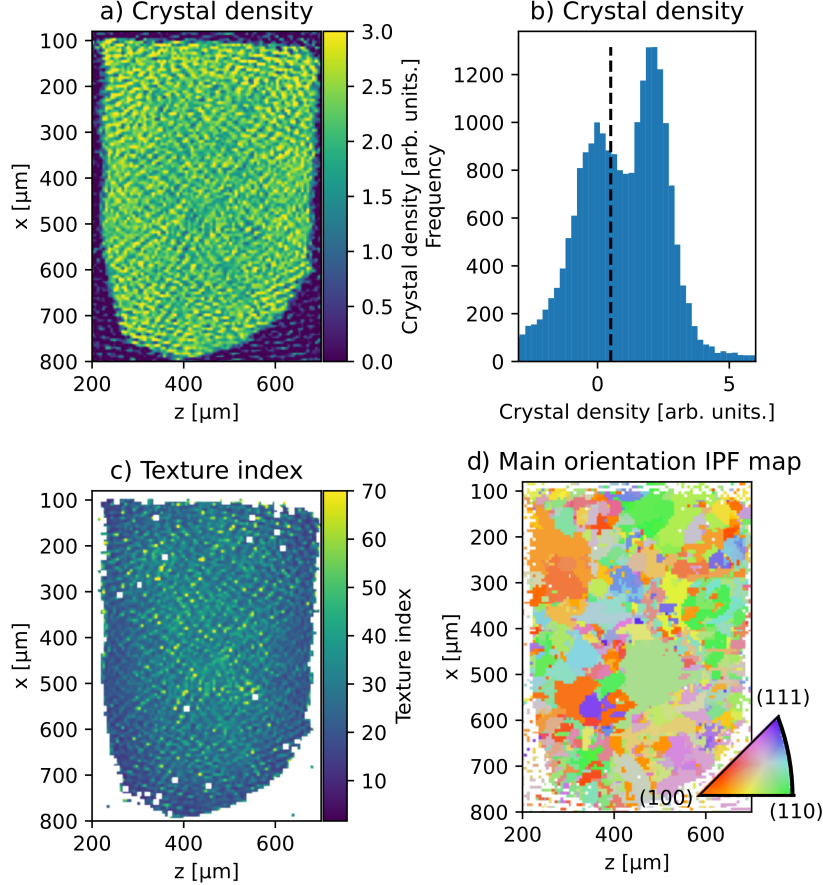
three-dimensional probe of local microstructure and strain. *Micron*, 35(6):431–439, 2004. International Wuhan Symposium on Advanced Electron Microscopy.

- [47] B. C. Larson and L. E. Levine. Submicrometre-resolution polychromatic three-dimensional X-ray microscopy. *Journal of Applied Crystallography*, 46(1):153–164, Feb 2013.
- [48] Can Yildirim, Carsten Detlefs, Albert Zelenika, Henning F. Poulsen, Raquel Rodriguez-Lamas, Philip K. Cook, Mustafacan Kutsal, and Nikolas Mavrikakis. Exploring 4d microstructural evolution in a heavily deformed ferritic alloy. *Journal of Physics: Conference Series*, 2635(1):012040, nov 2023.
- [49] Tianbo Yu, Chuanshi Hong, Yubin Zhang, Adam Lindkvist, Wenjun Liu, Jon Tischler, and Dorte Juul Jensen. Recovery of deformation microstructure in the bulk interior revealed by synchrotron x-ray micro-diffraction. *Materials Characterization*, 202:112997, 2023.
- [50] Frank Niessen, Tuomo Nyysönen, Azdiar A. Gazder, and Ralf Hielscher. Parent grain reconstruction from partially or fully transformed microstructures in MTEX. *Journal of Applied Crystallography*, 55(1):180–194, Feb 2022.

8 Supplementary

8.1 Importance of the non-negativity constraint

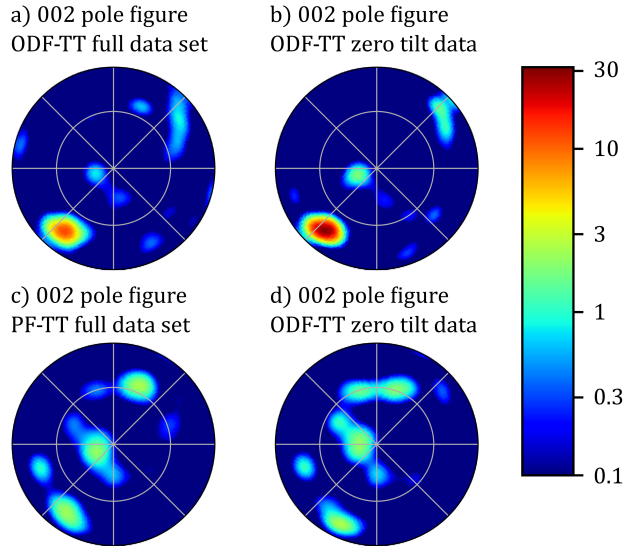
To illustrate the importance of the non-negativity constraint, we performed a reconstruction of the martensite data without using the non-negativity constraint. Figure S6 shows the results of this reconstruction. It is apparent, that the reconstruction without the non-negativity constraints suffers from a high-frequency reconstruction artifact which obfuscated many of the conclusions that were drawn from the data in the main manuscript.



Supplementary Figure S6: Tomograms of the martensite reconstruction without utilizing the non-negativity constraint. a) shows the reconstructed density and b) displays a histogram of the density values in a). b) shows the calculated texture index and d) shows a inverse pole figure map of the main orientation.

8.2 Comparison of pole-figures

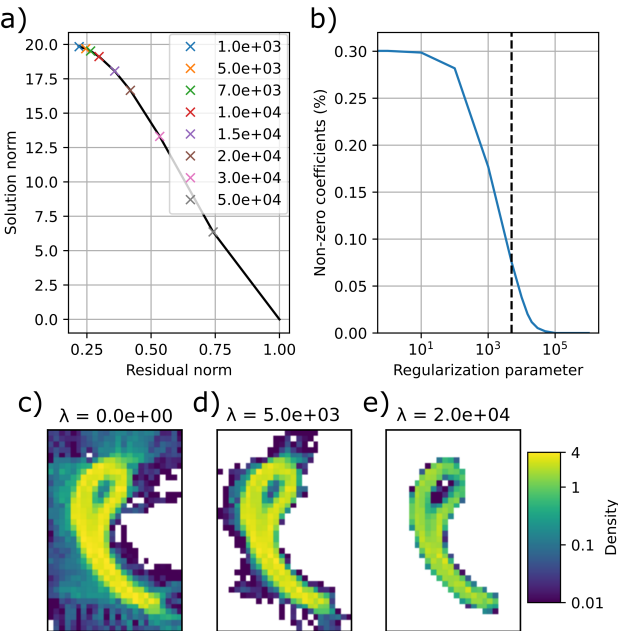
To give more insight into the comparison of ODF-TT and PF-TT, we plot the $\{200\}$ pole figure of a single voxel of the reconstructions of the gastropod shell data in Fig. S7. It appears that the PF-TT reconstruction do reconstruct significant scattering in the direction where ODF-TT has the majority of the intensity. However, the PF-TT reconstruction also has significant intensity in two other directions with similar amplitude.



Supplementary Figure S7: Pole-figures of a single voxel of the snail-sample with four different reconstructions.

8.3 L1 regularization

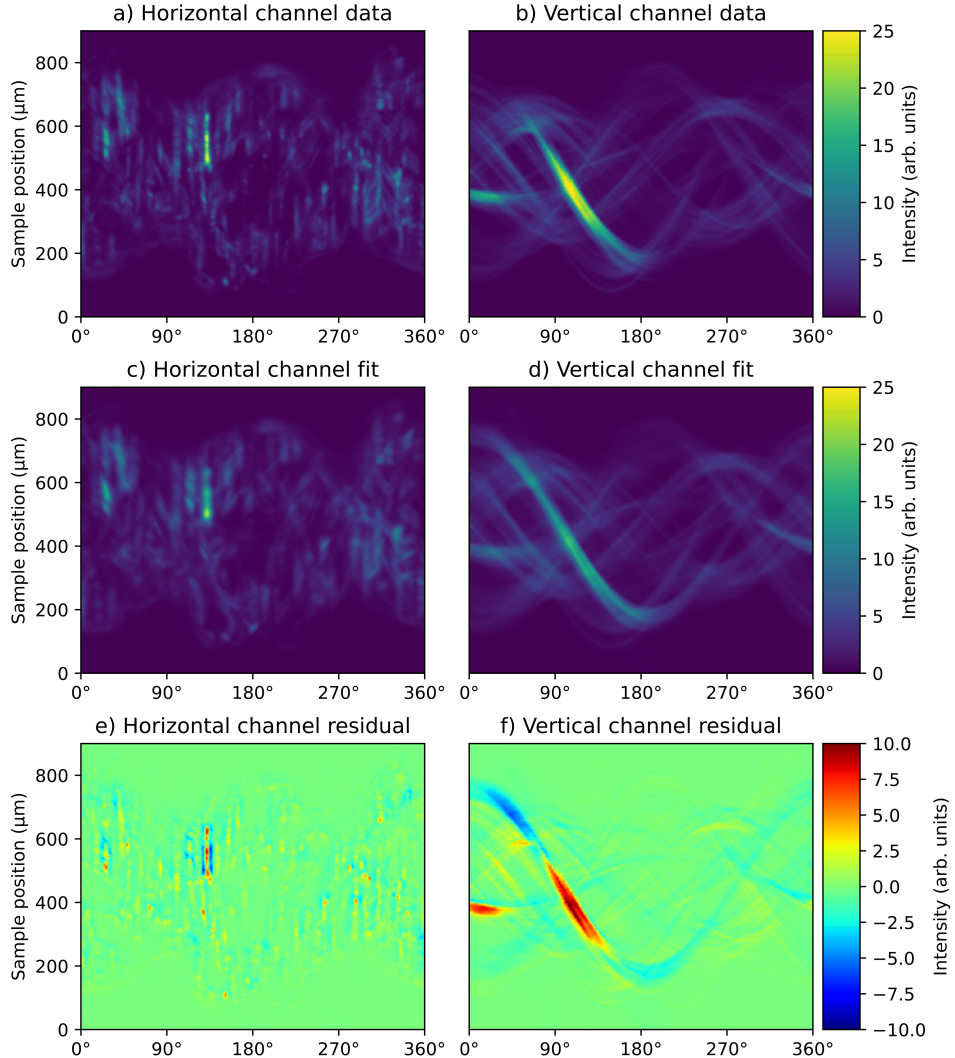
For the samples investigated in this paper, good reconstructions can be achieved without use of L1 regularization. There are however advantages to using the regularization. As seen in Fig. S8, using a regularized reconstruction can reduce streaking artifacts in the reconstruction and significantly decrease the number of non-zero coefficients. The latter is useful as it makes the reconstructed volumes easier to store and process for further analysis.



Supplementary Figure S8: Effect of regularization. a) Shows how the residual-norm and solution-norm depends on the choice of the regularization parameter λ . b) Percentage of non-zero coefficients as a function of regularization parameter. At $\lambda = 5 \cdot 10^3$ (dashed line) the number of non-zero coefficients have been reduced by about a factor of 4. Plots of the reconstructed density at c) $\lambda = 0.0$, d) $\lambda = 5 \cdot 10^3$, and d) $\lambda = 2 \cdot 10^4$. White regions in these images correspond to voxels where all coefficients are zero.

8.4 Residuals

To get some insight into the quality of the fit and potential source of errors, we show the fit and residuals in Fig. S9. The magnitude of the residual is lower than 2 throughout most of both sinograms, but peaks at a large value of around ± 10 near the most intense features in each sinogram. We believe that these large errors are due to the limited angular resolution of the reconstruction.



Supplementary Figure S9: Comparison of data and fit of the martensite reconstruction. a,b) experimental sinograms of the 110 peak for a single azimuthal detector channel. c,d) fitted sinograms of the same angular channel. e,f) residual. a,c,e) show an angular channel orthogonal to the rotation axis and b,d,f) show an angular channel parallel to the rotation axis.